Original Research Article

Analytical approximations for heat release rate laws in the time- and frequency-domains

Sreenath M Gopinathan ⓘ**, Alessandra Bigongiari** ⓘ **and
Maria Heckl** ⓘ

Abstract
This paper focusses on the relationship between the heat release rate and the acoustic field, which is a crucial element in modelling thermoacoustic instabilities. The aim of the paper is twofold. The first aim is to develop a transformation tool, which makes it easy to switch between the time-domain representation (typically a heat release law involving time-lags) and the frequency-domain representation (typically a flame transfer function) of this relationship. Both representations are characterised by the same set of parameters $n_1, n_2, \ldots, n_k$. Their number is quite small, and they have a clear physical meaning: they are time-lag dependent coupling coefficients. They are closely linked to the impulse response of the flame in the linear regime in that they are proportional to the discretised (with respect to time) impulse response. In the *nonlinear* regime, the parameters $n_1, n_2, \ldots, n_k$ become amplitude-dependent. Their interpretation as time-lag dependent coupling coefficients prevails; however, the link with the impulse response is lost. Nonlinear flames are commonly described in the frequency-domain by an amplitude-dependent flame transfer function, the so-called flame describing function. The time-domain equivalent of the flame describing function is sometimes mistaken for a 'nonlinear impulse response', but this is not correct. The second aim of this paper is to highlight this misconception and to provide the correct interpretation of the time-domain equivalent of the flame describing function.

1. Introduction

Power generation systems based on combustion of fuels to extract energy operate with *lean* premixed flames in order to reduce the environmental pollution by exhaust gases. However, such systems are susceptible to thermoacoustic instabilities that are characterised by high-amplitude oscillations caused by the feedback between oscillations in pressure and heat release rate. These oscillations lead to excessive vibration of structures and, in extreme cases, major hardware damage.

The relationship between the heat release rate and the acoustic field is a crucial element in modelling thermoacoustic instabilities. A common way to describe this relationship is by the flame transfer function (FTF), which is a frequency-domain concept, relating the (normalised) rate of heat release to the (normalised) acoustic velocity. The corresponding time-domain concept is the impulse response (IR), which can be obtained from the FTF by applying an inverse Fourier transform. The two descriptions contain exactly the same information,[1] but may serve different purposes: The FTF is frequently used in experimental settings because it is relatively straightforward to measure. The IR is more suitable for theoretical studies, where insight into the influence of time-delayed processes on the flame dynamics is a priority.

The FTF and IR are both linear concepts. They are valid if the response of the flame to an excitation with a given frequency and amplitude satisfies the following criteria:

1. the response does not contain any frequency other than the excitation frequency;

School of Chemical and Physical Sciences, Keele University, Keele, UK

Corresponding author:
Maria Heckl, School of Chemical and Physical Sciences, Keele University, Keele, UK.
Email: m.a.heckl@keele.ac.uk

2. the response amplitude is proportional to the excitation amplitude.

These criteria are satisfied if the velocity amplitude of the excitation is sufficiently small compared with the velocity of the mean flow.

High-amplitude oscillations are an important phenomenon in thermoacoustics. In order to model these, the concept of the flame describing function (FDF) was introduced by Noiray et al.[2] and has since then been used by a multitude of researchers in thermoacoustics.[3–6] The FDF is an extension of the FTF in that it also includes the dependence on the amplitude (not just frequency). However, it gives no information on new frequencies that might be generated by nonlinear effects. The FDF can be seen as a semi-nonlinear concept, which ignores the generation of new frequencies. Nevertheless, it is a powerful tool of great practical importance and has been used by many researchers to model nonlinear effects, such as limit cycle oscillations, hysteresis behaviour and mode hopping.[2,4,7–11]

Of course, it is possible to apply an inverse Fourier transform to any given FDF and transform it into the time-domain. However, the physical interpretation of this time-domain function is not obvious. Some authors regard it as an 'amplitude-dependent impulse response',[6,10] but this is misleading. In fact, this time-domain function is *not* an amplitude-dependent IR, if one takes the literal meaning: the response to an impulse with a given peak value (amplitude).

In the nonlinear regime, the direct correspondence between FDF and IR as Fourier transform pair no longer exists. This raises the following question: What is the physical meaning of the Fourier transform partner of the FDF? The current paper seeks to answer this question.

To this end we develop a transformation tool which makes it easy to switch between the time-domain and frequency-domain. In both domains, the same set of parameters appears in the mathematical representations. These parameters have a clear physical meaning, and their number is quite small (typically 10–20). Our starting point will be the well-known $n\tau$-law,[12] which relates the heat release rate linearly to a time-delayed velocity (time-lag τ) by a proportionality constant (coupling coefficient n). We extend the $n\tau$-law in two successive steps:

1. we introduce τ-dependent coupling coefficients involving a range of time-lags,
2. we introduce an additional amplitude-dependence.

Studies of time-lags and time-lag distributions go back to 2001. A comprehensive review can be found in Polifke.[13] In the five paragraphs below, we give a brief overview for the linear regime.

Polifke et al.[14] used Lagrangian particle tracking to find the histograms of fuel particles convected by the flow from the nozzle to the flame front. By investigating different nozzle geometries, they found that an elliptical premix nozzle produces a wider time-lag distribution with a smaller mean than other nozzles. The IR of a swirl burner studied by Huber and Polifke[15,16] clearly showed a distribution of time-lags around several central values. These IRs were responses to impulses in velocity and equivalence ratio.

Flohr et al.[17,18] showed an approach to calculate the FTF of a conical turbulent flame by assuming a time-lag mechanism. They used steady-state CFD to calculate the travel times of individual premix particles to reach the flame surface to derive the FTF. The distribution of their time-lags was a smooth curve, similar to a superposition of two Gaussians, centred around two peak values.

From the measured FTF of a swirl-stabilised industrial flame, Schuermans[19] developed a model with distributed time-lags. This model included the effects of flame shape, diffusion and distributed fuel injection. In a subsequent study of the same flame, Schuermans et al.[20] found that the distribution of time-lags is a superposition of two Gaussians. The position of the Gaussians along the time-lag axis turned out to correspond to two different transport phenomena: fluctuations in turbulence intensity and fluctuations in fuel concentration.

Komarek and Polifke[21] combined CFD with system identification to study a swirl burner for impulse excitation of the swirl number and velocity. They identified different transport mechanisms (convective and acoustic), and from this insight they developed a simple analytical model for the impulse response in terms of three Gaussian time-lag distributions, in both time- and frequency-domains.

There are also several studies by industrial researchers who have found time-lag laws and time-lag distributions. Krebs et al.[22] measured the response of a premixed swirl flame to forced pulsations of the burner flow and found that it almost follows a simple time-lag law. In the process of studying the acoustic energy generation by a premixed swirl burner, Gentemann and Polifke[23] considered a measured FTF and fitted a simple analytical model to it; this model featured a superposition of two Gaussian distributions and represented two transport phenomena with individual time-lags and dispersion. Kaess et al.[24] described a laminar premix flame with the same analytical model in order to perform a thermoacoustic stability analysis. Mensah et al.[25] performed a numerical study of the thermoacoustic modes in an

industrial annular combustion chamber; for the FTF they assumed a '$\sigma - \tau$' model, i.e. a single Gaussian distribution (width parameter σ, central time-lag τ) of time-lags. They then explored the effect of σ on the stability behaviour.

Studies of nonlinear flame dynamics with time-lag distributions and amplitude-dependence are relatively rare and recent.

Iurashev et al.[6] extended the approach by Komarek and Polifke[21] into the nonlinear domain. Their FDF data came from CFD simulations and comprised a total of 16 data points (four excitation frequencies with four excitation amplitudes). These data were approximated analytically by a superposition of three Gaussian functions with amplitude-dependent fitting parameters.

Gopinathan et al.[26] developed a conversion tool that is rooted in the time-domain. It involves a superposition of Gaussian distributions containing physically meaningful fitting parameters: prominent time-lags, as well as the width and height of the distributions around these time-lags. The same parameters appear in the frequency-domain representation, which is obtained analytically by Fourier transform. This frequency-domain representation is then fitted to given FDF data, and that way the amplitude-dependence of the fitting parameters is ascertained. The method works well if there is a small number of prominent time-lags (no more than five), but not if the time-lags are distributed fairly evenly. A classic case of evenly distributed time-lags is a long laminar flame. The dynamics of such a flame is determined by perturbations that travel from a reference position (typically the point where they are generated) to a particular location at the flame surface. This leads to an evenly distributed range of travel distances, and a corresponding evenly distributed range of time-lags.

Semlitsch et al.[10] calculated the FDF of flames described by the nonlinear G-equation, assuming several forcing mechanisms with different forcing frequencies and amplitudes. They then expressed these FDFs as a sum of time-lag terms with discrete time-lags. Each term included a 'time-delay constant' (similar to a coupling constant), which corresponded to a particular time-lag. In order to get good accuracy, it was necessary to include a large number of such terms (of the order of 800).

There is still a need for a method to determine an analytical approximation for a given flame response that satisfies the following requirements:

1. It makes no a-priori assumptions about prominent time-lags. This would address the limitation of the method in Gopinathan et al.[26]

2. It can be fitted to imperfect FTF or FDF data, such as data with poor frequency resolution. Methods based on the Fourier transform are not a good option in such a situation.

3. It has a relatively small number of fitting parameters so that it can be built into a larger analytical model (e.g. a network model) for a whole combustion system. An early attempt at such an analytical approximation can be found in Subramanian et al.,[27] who have used rational fitting functions with a small number of parameters; these functions are mathematically convenient, but have no physical basis, and give unreliable results.

As mentioned earlier, the current paper aims to get a physical understanding of the time-domain partner of the FDF. An associated aim is to present a new method by which a given FTF or FDF can be approximated with a simple analytical expression, while satisfying the requirements listed in the previous paragraph.

The paper is structured as follows. In Section 2, we will develop our transformation tool. This will turn out to have a practical advantage over the Fourier transform: it can be tailored to scenarios where the available FTF or FDF data are sparse and/or given at irregular frequency intervals. We will validate our transformation tool in Section 3, where we apply it to a laminar conical flame in the linear regime and use results from the G-equation as benchmark. The nonlinear regime is covered in Section 4. There we will demonstrate our transformation tool by applying it to a conical flame with two different models for the (high-amplitude) velocity field that excites the flame. A summary of the paper will be given in Section 5, together with conclusions and recommendations.

2. Transformation tool between time- and frequency-domain

2.1. Motivation

The procedure to convert a FTF, which is a frequency-domain relation, into a heat release rate law, which is a time-domain relation, is described in this section. We assume that the FTF is known a priori, obtained through measurements, numerical simulations or even from analytical expressions.

The rationale behind a heat release rate law with a distribution of time-lags is explained by the scenarios in Figure 1(a) and (b). Figure 1(a) shows flow perturbations travelling with *uniform* velocity towards an extended flame; the flow perturbations do not all cover the same distance and therefore arrive at the flame front at different time instances, leading to a distribution of time-lags in the flame response. Figure 1(b)
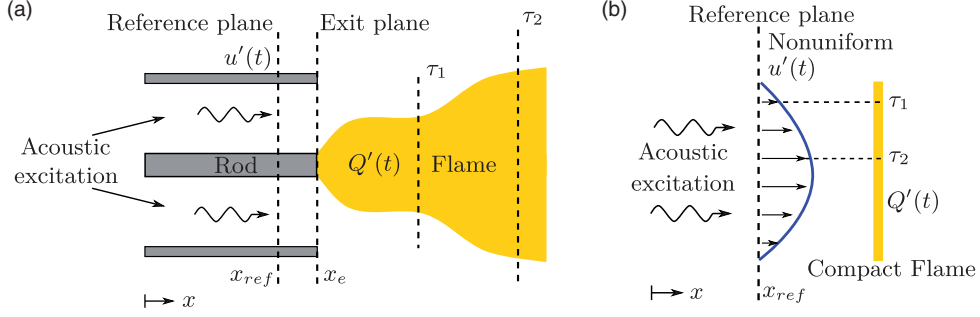
Figure 1. Mechanisms leading to a distribution of time-lags. (a) Extended flame; uniform velocity and (b) compact flame; non-uniform velocity.

shows the case of a (convectively) *compact* flame impinged on by flow perturbations with *non-uniform* velocity; again, there is a distribution of time-lags – in this case because of the different propagation velocities. Generally, any unsteady behaviour of the incoming mean flow can create a distribution of time-lags in the system. Since the local heat release rate fluctuations are functions of the local velocity fluctuations, the coupling coefficient n must be a function of the time-lag τ, and we denote this by $n(\tau)$.

A generalised heat release rate law in the time-domain can be written as

$$\frac{Q'(t)}{\bar{Q}} = \frac{1}{\tau_{char}} \int_{-\infty}^{\infty} n(\tau) \frac{u'(t-\tau)}{\bar{u}} \mathrm{d}\tau \quad (1)$$

where the (normalised) heat release rate fluctuations $(Q'(t)/\bar{Q})$ are related to the (normalised) acoustic velocity fluctuations $(u'(t-\tau)/\bar{u})$ through a generalised coupling coefficient n, which is not a constant, but a function of the time-lag τ. n is a real number and can have a positive or a negative value. τ_{char} is a characteristic time of the system, for example, the time taken by the disturbance to travel from the base of the flame to its tip.

Owing to the causality condition, the heat release rate fluctuations cannot occur before their cause (i.e. the velocity perturbation), so only positive time-lags are possible, and the lower integration limit in equation (1) must be zero. For the upper limit, we assume that there is a finite value τ_{max} which corresponds to the maximum delay between the impulse (acoustic fluctuations at the reference plane) and its response (heat release rate fluctuations at the flame). In our analysis, we use the maximum time-delay as the characteristic time. Therefore, equation (1) can now be written as

$$\frac{Q'(t)}{\bar{Q}} = \frac{1}{\tau_{max}} \int_0^{\tau_{max}} n(\tau) \frac{u'(t-\tau)}{\bar{u}} \mathrm{d}\tau \quad (2)$$

The corresponding FTF is obtained by Fourier transforming equation (2) and then rearranging it in
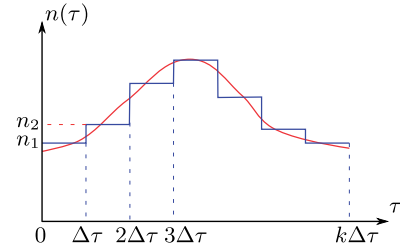
Figure 2. Schematic representation of the piecewise approximation of the coupling coefficient.

the form of a ratio of normalised heat release rate fluctuations to normalised velocity fluctuations in the frequency-domain.

Though at this stage, we do not know the dependence of n on τ, we proceed with our analysis by assuming that such a dependence exists. We assume a hypothetical $n(\tau)$ as illustrated by the red curve in Figure 2, and approximate it by a piecewise constant function illustrated by the blue curve. The integration range $[0, \tau_{max}]$ has been divided into k equal intervals of width $\Delta\tau$, and n is uniform in each of these intervals.

Using this piecewise constant function for $n(\tau)$, we can approximate the integral in equation (2) as a sum of k integrals, i.e.

$$\frac{Q'_k(t)}{\bar{Q}} = \frac{1}{\tau_{max}} \left[n_1 \int_0^{\Delta\tau} \frac{u'(t-\tau)}{\bar{u}} \mathrm{d}\tau + n_2 \int_{\Delta\tau}^{2\Delta\tau} \frac{u'(t-\tau)}{\bar{u}} \mathrm{d}\tau \right.$$
$$\left. + \cdots + n_k \int_{(k-1)\Delta\tau}^{k\Delta\tau} \frac{u'(t-\tau)}{\bar{u}} \mathrm{d}\tau \right]$$
$$(3)$$

where $Q'_k(t)$ denotes the approximation of $Q'(t)$ by k terms. The parameters τ_{max} and $\Delta\tau$ are deduced from the given FTF according to a selection procedure described in Section 2.4. It should be noted that the only unknowns in equation (3) are the coupling coefficients $n_1, n_2, \ldots, n_k$. These coefficients are determined from the given FTF through an error minimisation technique, as described in Section 2.2.

Since equation (3) is an approximation of the heat release rate law in the time-domain, its Fourier transform is an equivalent approximation in the frequency-domain. The Fourier transform, when performed analytically for each individual integral (see Appendix 1), leads to

$$\frac{\hat{Q}_k(\omega)}{\bar{Q}} = \left\{ \frac{1}{\tau_{\max}} e^{-i\omega\frac{\Delta\tau}{2}} \frac{2}{\omega} \sin\left(\omega\frac{\Delta\tau}{2}\right) \left[n_1 e^{i\omega\Delta\tau} + n_2 e^{2i\omega\Delta\tau} + \cdots + n_k e^{ki\omega\Delta\tau} \right] \right\} \frac{\hat{u}(\omega)}{\bar{u}}$$

(4)

The analytical expression for the FTF from equation (4) is

$$\begin{aligned} \mathcal{T}_k(\omega) &= \frac{\hat{Q}_k(\omega)}{\bar{Q}} \bigg/ \frac{\hat{u}_k(\omega)}{\bar{u}} \\ &= \frac{1}{\tau_{\max}} e^{-i\omega\frac{\Delta\tau}{2}} \frac{2}{\omega} \sin\left(\omega\frac{\Delta\tau}{2}\right) \bigg[n_1 e^{i\omega\Delta\tau} + n_2 e^{2i\omega\Delta\tau} \\ &\quad + \cdots + n_k e^{ki\omega\Delta\tau} \bigg] \end{aligned}$$

(5)

where $\mathcal{T}_k(\omega)$ denotes the FTF corresponding to equation (3). We will refer to it from now on as the 'analytical approximation'.

2.2. Method to determine the coupling coefficients

The coupling coefficients n_1, n_2, ..., n_k are determined by minimising the discrepancy between the original FTF, $\mathcal{T}(\omega)$ and its analytical approximation, $\mathcal{T}_k(\omega)$. We express this discrepancy by the mean square error (MSE), given by

$$\epsilon_k = \frac{1}{\omega_{\max}} \int_0^{\omega_{\max}} [\mathcal{T}(\omega) - \mathcal{T}_k(\omega)]^2 \mathrm{d}\omega$$

(6)

in the frequency range $[0, \omega_{\max}]$, where $\omega_{\max}$ is taken as the maximum angular frequency for which the FTF data are available. In practice, FTFs tend to decay strongly beyond a certain cut-off frequency (low-pass filter), and often FTF data are available for the whole frequency range of interest, i.e. above this cut-off frequency. Since the MSE in equation (6) is integrated over ω, the number of parameters k is not limited by the number of data points available in the range $[0, \omega_{\max}]$. However, a higher number of data points will improve the output of the MSE minimisation. A generic example of an FTF is shown in Figure 3, with the gain plotted in Figure 3(a) and the phase in Figure 3(b). The markers symbolise the data available, and using these data we intend to evaluate the coupling coefficients n_1, n_2, ..., n_k by the minimisation of the
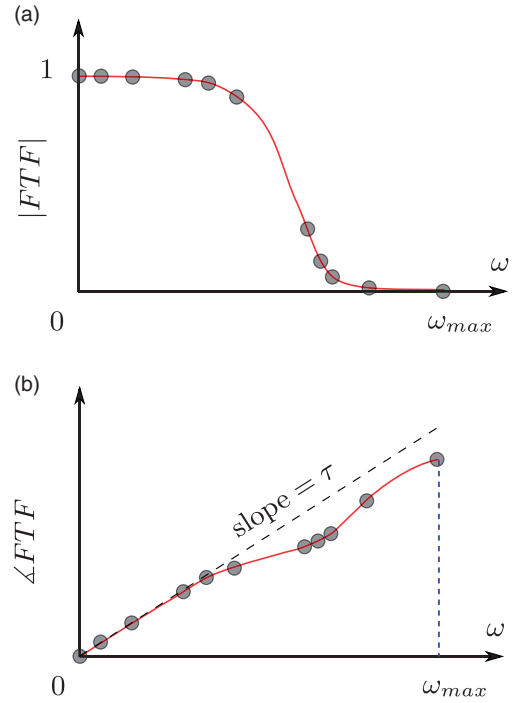
Figure 3. Gain and phase of a generic FTF. (a) Gain and (b) phase. Markers: mock data. FTF: flame transfer function.

MSE. The minimisation is done with respect to the coupling coefficients, i.e. we evaluate $\partial\epsilon_k/\partial n_1 = 0$, $\partial\epsilon_k/\partial n_2 = 0$, ..., $\partial\epsilon_k/\partial n_k = 0$. This leads to a set of k simultaneous equations that can be represented in matrix form as

$$\begin{bmatrix} A_{11} & A_{12} & \cdots & A_{1k} \\ A_{21} & A_{22} & \cdots & A_{2k} \\ \vdots & \vdots & \ddots & \vdots \\ A_{k1} & A_{k2} & \cdots & A_{kk} \end{bmatrix} \begin{bmatrix} n_1 \\ n_2 \\ \vdots \\ n_k \end{bmatrix} = \begin{bmatrix} B_1 \\ B_2 \\ \vdots \\ B_k \end{bmatrix}$$

(7)

The matrix elements A_{pq} and the vector elements B_p are given by

$$A_{pq} = \int_0^{\omega_{\max}} |\Phi(\omega)|^2 \cos(|p-q|\omega\Delta\tau) \mathrm{d}\omega, \quad p, q = 1, \ldots, k$$

(8)

and

$$B_p = \int_0^{\omega_{\max}} \Re\{\mathcal{T}(\omega)\Phi^*(\omega)e^{-pi\omega\Delta\tau}\} \mathrm{d}\omega, \quad p = 1, \ldots, k$$

(9)

where

$$\Phi(\omega) = \frac{1}{\tau_{\max}} e^{-i\omega\frac{\Delta\tau}{2}} \frac{2}{\omega} \sin\left(\frac{\omega\Delta\tau}{2}\right)$$

(10)

and $\Phi^*(\omega)$ is its complex conjugate. These elements are best calculated numerically (e.g. by using the trapezoidal rule).

2.3. Comparison of n(τ) distribution and IR

The FTF $\mathcal{T}(\omega)$ is the frequency-domain representation, and the unit IR, $h(t)$ is the time-domain representation of the flame dynamics.[1] For a linear flame, they are directly related by Fourier transform: $\mathcal{T}(\omega) = \mathscr{F}[h(t)]$. Our time-lag distribution $n(\tau)$ is directly proportional to the unit IR; this can be seen by applying an impulsive velocity excitation

$$\frac{u'(t - \tau)}{\bar{u}} = \delta(t - \tau) \qquad (11)$$

to the flame described by equation (1)

$$h(t) = \int_{-\infty}^{\infty} \frac{n(\tau)}{\tau_{\max}} \delta(t - \tau) \mathrm{d}\tau = \frac{n(t)}{\tau_{\max}} \sim n(t) \qquad (12)$$

In the nonlinear regime, the situation is less straightforward. The FDF $\mathcal{T}(\omega, a)$ (a is the amplitude of the excitation velocity) is a simplified frequency-domain representation of the flame dynamics in that new frequencies generated by nonlinear effects are ignored. Our time-lag distribution $n(\tau)$ is the time-domain representation of this simplified flame description. This is not to be confused with the true IR of a nonlinear flame.

2.4. Practical considerations for the choice of τ_{max} and $\Delta\tau$

The quantities τ_{max} and $\Delta\tau$ have to be chosen carefully, and in this section we give guidelines on how to safeguard against spurious results.

As explained in Section 2.1, we assume that $\tau_{\max}$ is the maximum time-delay between the impulse and its response. This is a finite time interval. In many cases, $\tau_{\max}$ is the time it takes an impulse to travel from the base of the flame to the tip of the flame; an example is the laminar linear flame studied by Blumenthal et al.[28] However, $\tau_{\max}$ can be larger than the travel time along the flame; an example is the flame studied by Albayrak et al.,[29] where dispersion prolongs the flame response. In any case, $\tau_{\max}$ is within a range, which has a definite lower bound and some finite upper bound.

Information about travel times is often not available, and then the question arises how $\tau_{\max}$ can be determined just from the FTF or FDF data. An initial estimate for $\tau_{\max}$ can be obtained from the slope of the phase curve of the FTF near $\omega = 0$ (see dashed line in Figure 3(b)). If the resulting $\mathcal{T}_k(\omega)$ does not match the original FTF, then this is a sign that the initial $\tau_{\max}$ was an underestimate, and the calculation should then be repeated with a higher value. If the $\mathcal{T}_k(\omega)$ resulting from the initial estimate for $\tau_{\max}$ *does* match the original FTF well, then this initial estimate may either be a good value or an overestimate. An easy way to check this is to examine the n_k values resulting from the approach described in Section 2.1. If these are zero beyond a certain k value $k_{\max}$, then this is an indication that $\tau_{\max}$ can be reduced to $k_{\max}\Delta\tau$.

The time interval $\Delta\tau$ also needs to be chosen with care – in order to avoid aliasing. This phenomenon can occur when a finite number of data points are transformed between the frequency-domain and the time-domain. It manifests itself by a distortion of the transformed data and is due to a mismatch between the highest frequency in the signal and the sampling interval in the time-domain. The Nyquist theorem gives a criterion to avoid this mismatch: the sampling frequency, $F_s = 1/\Delta t$ (Δt is the sampling interval) has to satisfy

$$F_s \geq 2 \times f_{\max} \qquad (13)$$

$f_{\max}$ is the maximum frequency for which FTF data are available and it corresponds to the angular frequency $\omega_{\max}$ appearing in equation (6) and Figure 3. The sampling interval Δt has to satisfy

$$\Delta t \leq \frac{1}{2 f_{\max}} \qquad (14)$$

and hence our time-lag interval $\Delta\tau$ must not be less than Δt.

3. Validation against a linear conical flame

3.1. Test data

In order to illustrate our method, we apply it to a fundamental flame: a conical flame which is perfectly premixed and laminar. Conical flames have been studied by several researchers, most notably by Schuller et al.[30] who solved the G-equation analytically and derived explicit expressions for the FTFs. Using these FTFs, we will now validate our method by evaluating the approximations to the FTFs and subsequently by estimating the corresponding heat release rate laws.

Conical flames are formed when the flame (or the combustion zone) anchors on the rim of a circular burner. This is illustrated schematically in Figure 4. Since the burner set-up is axisymmetric, only one half of the cross-section is shown. Here, $\bar{u}$ is the mean flow velocity of the fuel–air mixture, S_L is the laminar flame speed (which is a constant for a given mixture) and R is the radius of the burner. The steady-state position of

the flame is determined by the kinematic balance between the laminar flame speed S_L and the flame-normal component $\bar{V}$ of the mean flow velocity $\bar{u}$; the half-angle α of the flame is given by $\alpha = \sin^{-1}(S_L/\bar{u})$. Small flame angles represent long pointed flames and large flame angles represent short flames, and as the flame angle tends to 90°, the flame becomes flat.

Schuller et al.[30] found the FTFs of conical flames subjected to a convective velocity perturbation

$$u(y, t) = \bar{u}[1 + \epsilon \sin(\omega t - ky)] \tag{15}$$

$$v(y, t) = 0 \tag{16}$$

where the convecting wave travels from the base of the flame to its tip with a wavenumber $k = \omega/\bar{u}$, and ϵ is the amplitude of the velocity perturbation. This is an
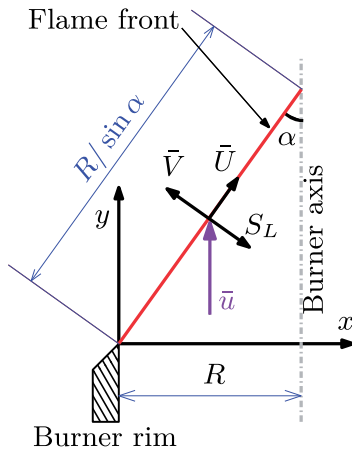
Figure 4. Schematic representation of a conical flame.

axial convective velocity perturbation where the velocity fluctuation in the radial direction is not considered. The corresponding FTF is given by[30]

$$\mathcal{T}(\omega)_{\text{conical}} = \frac{2}{\omega_*^2} \frac{1}{1 - \cos^2\alpha} \left[1 - \exp(i\omega_*) + \frac{\exp(i\omega_* \cos^2\alpha) - 1}{\cos^2\alpha} \right] \tag{17}$$

where $\omega_* = \omega R/(S_L \cos\alpha)$ is called the reduced frequency.

The test data ($\mathcal{T}(\omega)_{\text{conical}}$) for a conical flame of radius $R = 11$ mm and a flame speed $S_L = 0.39$ m/s were generated for 20 data points at regular intervals for a range of reduced frequencies ($\omega_* = 0.1, \ldots, 100$) and for three different flame angles ($\alpha = 20°$, 45° and 88°).

3.2. Results from our method in the time- and frequency-domain

We apply our analytical approximation to the FTFs of conical flames given in equation (17). The parameters τ_{max} and $\Delta\tau$ described in Section 2.4 are evaluated from the original FTFs with the value of τ_{max} chosen to be the time taken by a uniform velocity perturbation to travel along the flame front (characteristic time of conical flame), given by $\tau_{pert} = R/(S_L \cos\alpha)$[28] and divided into 16 divisions ($\Delta\tau = \tau_{\text{max}}/16$). The number of divisions was chosen according to the criteria described in Section 2.4. The analytical approximation of the FTFs of the form shown in equation (5) and their corresponding $n(\tau)$ distributions for conical flames subjected to the perturbations described in equations (15) and (16) are shown in Figure 5(a) to (c) for three different flame angles $\alpha = 20°$, 45° and 88°. The gain of the FTF (Figure 5(a)) and the phase of the FTF (Figure 5(b)) are plotted against the reduced frequency ω_*, where the
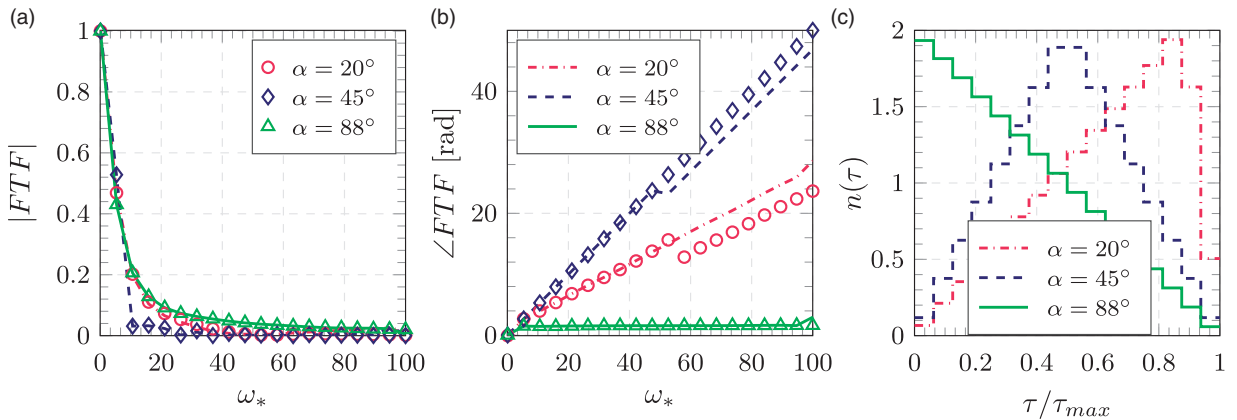
Figure 5. Results for the conical flame with different flame angles α subjected to convective perturbation. (a) Gain and (b) phase of the FTF as a function of ω_* and (c) time-lag distribution. In figures (a) and (b), markers represent the gain and phase of the FTF calculated using equation (17) and the curves represent the gain and phase of the FTF calculated using the analytical approximation. FTF: flame transfer function.

markers denote the FTF data obtained using equation (17) and the curves denote the analytical approximation ($\mathcal{T}_k$). The plots show that there is good agreement between the two data sets.

The $n(\tau)$ distributions associated with the analytical approximation of FTFs for the conical flame and three flame angles are plotted in Figure 5(c), where the x-axis is the time-lag normalised with respect to $\tau_{\max}$. We observe that the overall trend in the $n(\tau)$ distribution is such that at first the value of n increases with increasing $\tau/\tau_{\max}$, reaches a maximum, and then decreases. For small flame angles, the peak in the $n(\tau)$ distribution is at a larger time-lag, and the peaks shift towards smaller time-lags as the flame angle increases. The peak in the $n(\tau)$ distribution points to the most prominent time-lag associated with the flame and can be considered as the time taken for any perturbation, originating at the burner rim to convect along the full length of the flame front. Small flame angles represent long flames and hence the time-lags will be larger. This is the reason why the peaks in the $n(\tau)$ distribution shift towards smaller time-lags as the flame angle increases. For flame angles close to 90° (e.g. $\alpha = 88°$), the convective time is very small and therefore the effects of convective perturbation are not visible in the $n(\tau)$ distribution. Detailed explanations and physical insight into the flame dynamics can be found in Blumenthal et al.[28] and Preetham et al.[31]

4. Application to a conical flame in the nonlinear regime

4.1. Background

So far in our analysis, we had considered only linear flames where only one FTF existed for every flame, irrespective of the amplitude of the exciting velocity fluctuation. In this section, we extend our analysis and apply the proposed analytical approximation to *nonlinear* flames that are characterised by a FDF, i.e. by a collection of FTFs for different amplitudes of excitation.

In order to illustrate the application of our analytical approximation to a FDF, we consider a conical flame described by the *nonlinear* G-equation. We generate the test data with the G-equation solver tool GFLAME[32] for a range of frequencies ($\omega_* = 0, \ldots, 80$) and a range of amplitudes ($\epsilon = 0.02, \ldots, 0.68$), where $\epsilon = a/\bar{u}$ is the ratio between velocity amplitude and mean flow velocity. The flame is a methane/air flame described by the following parameters: $\phi = 0.95$ (equivalence ratio), $R = 12.5$ mm (radius of the tube anchoring the flame or the flame base radius), $\bar{u} = 1.26$ m/s (mean flow velocity upstream of the flame); the flame angle for this case is $\alpha = 18.1°$. These parameters simulate the flame studied

experimentally by Karimi et al.,[33] who provided physical insight into the nonlinear mechanisms of their flame; we will refer to that in the next sections. We consider only fluctuations in velocity and neglect fluctuations in quantities like equivalence ratio and curvature dependent flame speed (for details see Lieuwen[34]). In the nonlinear regime, we apply our analytical approximation to flames subjected to two different velocity perturbations, 1-D and 2-D velocity fields. Using the FDF obtained from GFLAME, we now construct the corresponding analytical approximations of the FDFs obtained for the two velocity models.

4.2. Flame excited by 1-D velocity field

Our analytical approximation is first applied to a FDF using a 1-D velocity model that considers axial velocity perturbations given by equations (15) and (16). The gain and phase from GFLAME and the analytical approximation for this velocity model are compared in Figure 6(a) and (b), respectively. The markers denote the simulation results from GFLAME and the curves denote their corresponding analytical approximations. The plots show good agreement between the original FDF and the analytical approximation of FDF. However, the phase predicted for higher ω_* at high ϵ shows some deviation from the simulation values.

The $n(\tau)$ distribution of the FDF is plotted in Figure 6(c) where the x-axis shows the time-lags and the y-axis shows the coupling coefficient $n(\tau)$. The thin dotted lines represent the discretised or the piecewise $n(\tau)$ distribution obtained using our analytical approximation and the solid curves represent their smoothened version to highlight the shape of the $n(\tau)$ distribution.

The number of divisions k (in equation (3)) in $\tau_{\max}$ is taken as 24 ($\Delta\tau = \tau_{\max}/24$) and this satisfies the criteria described in Section 2.4. The value of $\tau_{\max}$ was chosen in a two-step procedure: first, the $n(\tau)$s were calculated with $\tau_{\max} = \tau_{pert} = R/(S_L\cos\alpha)$, but this value of $\tau_{\max}$ did not produce a good approximation of the FTFs. The value of $\tau_{\max}$ was then increased to $2R/(S_L\cos\alpha)$, which gave good approximations of all the individual FTFs shown in Figure 6. From Figure 6(c), we observe that the $n(\tau)$s, when compared to the distribution in Figure 5(c), have dispersion[29] as the amplitude ϵ increases, i.e. the time instant beyond which $n(\tau)$ remains zero increases with amplitude as opposed to the fixed value of $\tau_{pert} = R/(S_L\cos\alpha)$ in Figure 5(c). Therefore, we have to choose a higher $\tau_{\max}$ that encompasses the whole range of dispersed $n(\tau)$s. The discrepancy in the phase at ω_* values above 20 is due to the low gain (close to zero) at these ω_* values which make the phase calculations quite inaccurate.
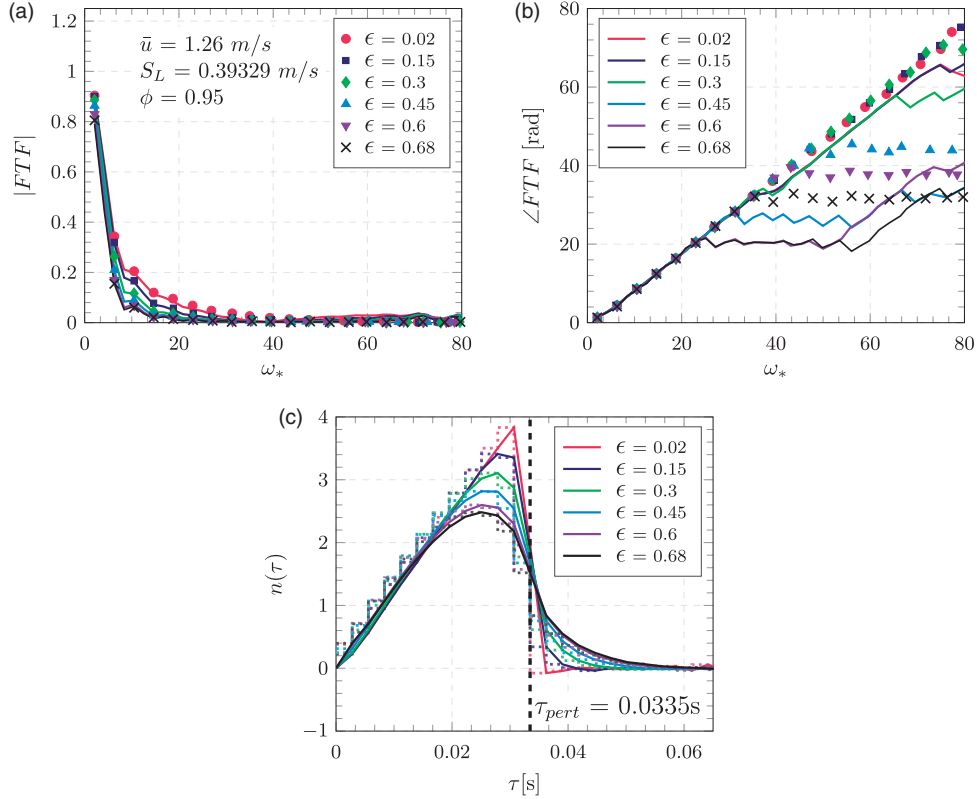
Figure 6. Results for the conical flame with different amplitudes ϵ of the 1-D velocity excitation model. (a) Gain and (b) phase of the FTF as a function of ω_* and (c) time-lag distribution. In figures (a) and (b), markers represent the gain and phase of the FDF from GFLAME and the curves represent the gain and phase of the FDF calculated using the analytical approximation. The flame angle is $\alpha = 18.1°$. FTF: flame transfer function; FDF: flame describing function.

4.3. Flame excited by 2-D velocity field

In this section, we apply our analytical approximation to a FDF using the 2-D velocity model that considers both the axial *and* radial perturbations in the velocity. Here, the axial velocity perturbation is given by equation (15) and the radial component $v(y, t)$ is determined by solving the incompressible continuity equation

$$\frac{\partial v}{\partial x} + \frac{\partial u}{\partial y} = 0 \qquad (18)$$

Figure 7(a) and (b) shows the gain and phase of the FTFs for this 2-D velocity model at the different amplitudes considered. The markers denote the simulation results from GFLAME and the curves denote their corresponding analytical approximations. The plots show good agreement between the original FDF and the analytical approximation. An exception is the phase at ω_* values above about 45 for $\epsilon = 0.02$ where the analytical approximation over-predicts the phase. This is due to the low gain values at those ω_* as discussed in the 1-D velocity case. Nevertheless, the agreement is very good

for low ω_* values. The $n(\tau)$ distribution of the FDF is plotted in Figure 7(c) and in this figure too, the thin dotted lines represent the discretised or the piecewise $n(\tau)$ distribution obtained using our analytical approximation and the solid curves represent their smoothened version to highlight the shape of the $n(\tau)$ distribution. We use $\tau_{\max} = 2R/(S_L \cos \alpha)$ for the 2-D velocity model also, as discussed in Section 4.2.

4.4. Discussion

For the lowest amplitude considered ($\epsilon = 0.02$) in the 1-D velocity model, the $n(\tau)$ in Figure 6(c) has a behaviour similar to that of the linear $n(\tau)$ obtained for $\alpha = 20°$ in Figure 5. For higher amplitudes, we observe both dispersion as well as a reduction of the peak of $n(\tau)$ as ϵ increases. The peak of the $n(\tau)$ curves in Figure 6(c) shifts to lower time-lags as ϵ increases. The $n(\tau)$ for $\epsilon = 0.02$ for the 1-D velocity model in Figure 6(c) is comparable to the linear results in Figure 5. However, the $n(\tau)$ distributions for the 1-D velocity model and the 2-D velocity model are not comparable
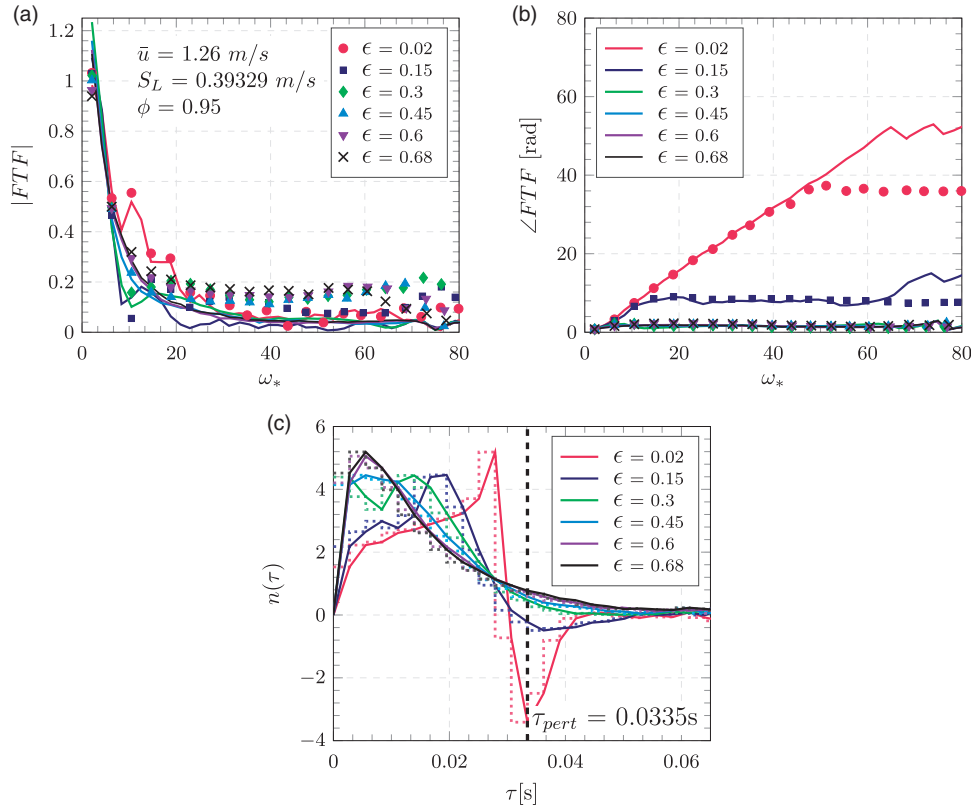
Figure 7. Results for the conical flame with different amplitudes ϵ of the 2-D velocity excitation model. (a) Gain and (b) phase of the FTF as a function of ω_* and (c) time-lag distribution. In figures (a) and (b), markers represent the gain and phase of the FDF from GFLAME and the curves represent the gain and phase of the FDF calculated using the analytical approximation. The flame angle is $\alpha = 18.1°$. FTF: flame transfer function; FDF: flame describing function.

due to the axial velocity component in the 2-D velocity model.

For the two low-amplitude cases in the 2-D velocity model, $\epsilon = 0.02$ and 0.15, $n(\tau)$ in Figure 7(c) increases initially with τ, reaches a maximum, switches sign to a negative minimum and then increases to zero as τ approaches τ_{max}. For all other ϵ values, $n(\tau)$ in Figure 7(c) increases initially and then decreases gradually to zero as τ approaches τ_{max}. It can also be observed that the peak value of $n(\tau)$ moves to lower time-lags as the perturbation amplitude increases. This behaviour of $n(\tau)$ can be explained with the experimental observations of Karimi et al.[33] (in Figure 14 and Section 3.3.2 of their paper). In a conical flame, any distortions of the flame front have the greatest impact near the flame *tip*, where flame front sections are very close to one another. The flame tip is associated with the longest travelling times and the largest time-lags. As the amplitude of the flame front distortions increases, their impact spreads to regions, where the flame is wider and which take less time to reach than the flame tip. As a result, the prominent time-lags shift to lower values as the amplitude is increased. This feature is

captured well by our analytical approximation and is evident in Figure 7(c). Another trend in the flame behaviour was observed by Karimi et al.[33] when they increased the frequency of the perturbations, while keeping the amplitude constant. An increase in frequency leads to a more curvy flame surface. Again, the impact, which is greatest at the flame tip, spreads to wider regions of the flame that are reached more quickly by the perturbations. This phenomenon leads to a saturation of the phase of the FTF as the frequency is increased. Our analytical approximation captures this effect well, as can be seen in Figure 7(b).

Therefore, the $n(\tau)$ distribution predicted using our analytical approximation gives good insight into the behaviour of the flame in the nonlinear regime and also the behaviour in the linear regime as discussed in Section 3.2. Our analytical approximation captures the key flame dynamics which can now be easily incorporated into low-order network models, both in the frequency as well as in the time-domain. This in turn facilitates faster stability predictions and parametric studies in combustion systems prone to thermoacoustic instabilities.

5. Conclusions

The well-known $n\tau$-law, $\frac{Q'(t)}{\bar{Q}} = n\frac{u'(t-\tau)}{\bar{u}}$, and corresponding FTF, $\mathcal{T}(\omega) = ne^{i\omega\tau}$, describe the flame response in terms of a single time-lag τ and coupling coefficient n. We extended this description by introducing multiple time-lags with corresponding coupling coefficients n_1, n_2, n_3, …. The coupling coefficients form a set of parameters that appear both in the time-domain and frequency-domain description, and they provide analytical expressions for the flame response. We introduced a tool with which these analytical expressions can be determined, from FTF data in terms of gain and phase at a range of frequency values (obtained, for example, from experiment). This description is physically meaningful in that it captures transport phenomena and their effect on the flame response. We validated our method by applying it to a laminar conical flame, the FTF of which is known,[30] and found that it was very accurate. We subsequently applied it in the nonlinear regime, to study the flame response to excitation not only with different frequencies, but also with different *amplitudes*. Test data were generated numerically, in form of a FDF, using the code GFLAME.[32,35,36] Our method then gave us an analytical approximation of the GFLAME results, both in the time- and frequency-domain. The time-domain results revealed that the set of coupling coefficients n_1, n_2, n_3, … is dependent on the amplitude of excitation. From this we gained insight into how the excitation amplitude affects the flame response. In particular, we observed that the peak in the $n(\tau)$ curve shifts to lower τ-values as the amplitude was increased; this suggests that transport phenomena take place over shorter distances.

Incidentally, our findings from GFLAME are in line with the experimental observations by Karimi et al.,[33] who visualised a laminar conical flame, which they had excited with various frequencies and amplitudes. Our description of the nonlinear flame response in terms of amplitude-dependent coupling coefficients offers new physical insight into experimental observations, such as those in Karimi et al.[33]

Our approach provides a convenient tool to find analytical expressions for a nonlinear flame response; this is useful in several situations:

- The flame response can be incorporated easily into low-order models, in order to make stability predictions of thermoacoustic systems.
- If FDF data are missing for certain amplitude or frequency values, the gaps in the data can be interpolated in a natural way.
- It is also possible to extrapolate FDF data to large frequency and amplitude values.

However, the method introduced in this paper is more than a convenient modelling tool: it also provides a physical interpretation of the time-domain equivalent of the FDF. The current understanding of nonlinear flame responses in the time-domain is incomplete: in the linear regime, the IR is the time-domain equivalent of the FTF; in the nonlinear regime, however, this equivalence is lost. The gap is filled by our representation of the flame response by time-lag dependent coupling coefficients. We have demonstrated that this representation is equal (apart from a constant factor) to the IR in the linear regime, we have extended it to the nonlinear regime and we have shown that it is the time-domain equivalent of the FDF. Moreover, our representation is physically meaningful in that it gives insight into how the amplitude of excitation modifies transport processes. We therefore expect that our method can be applied to any flame whose response is affected by convected perturbations.

Declaration of Conflicting Interests

The author(s) declared no potential conflicts of interest with respect to the research, authorship, and/or publication of this article.

ORCID iDs

Sreenath M Gopinathan https://orcid.org/0000-0003-4595-699X
Alessandra Bigongiari https://orcid.org/0000-0003-2401-5429
Maria Heckl https://orcid.org/0000-0002-0192-7508

References

1. Polifke W, Poncet A, Paschereit CO, et al. Reconstruction of acoustic transfer matrices by instationary computational fluid dynamics. *J Sound Vib* 2001; 245: 483–510.
2. Noiray N, Durox D, Schuller T, et al. A unified framework for nonlinear combustion instability analysis based on the flame describing function. *J Fluid Mech* 2008; 615: 139–167.

3. Illingworth SJ and Juniper MP. When will a flame describing function approach to thermoacoustics work well? In: *Proceedings of the 19th International Congress on Sound and Vibration*, Vilnius, Lithuania, 8–12 July 2012.

4. Ćosić B, Terhaar S, Moeck JP, et al. Response of a swirl-stabilized flame to simultaneous perturbations in equivalence ratio and velocity at high oscillation amplitudes. *Combust Flame* 2015; 162: 1046–1062.

5. Han X and Morgans AS. Simulation of the flame describing function of a turbulent premixed flame using an open-source LES solver. *Combust Flame* 2015; 162: 1778–1792.

6. Iurashev D, Campa G, Anisimov VV, et al. Three-step approach for prediction of limit cycle pressure oscillations in combustion chambers of gas turbines. *Combust Theory Model* 2017; 21: 1148–1175.

7. Moeck JP and Paschereit CO. Nonlinear interactions of multiple linearly unstable thermoacoustic modes. *Int J Spray Combust Dyn* 2012; 4: 1–27.

8. Boudy F, Schuller T, Durox D, et al. The flame describing function (FDF) unified framework for combustion instability analysis: progress and limitations. In: n^3l – *International Summer School and Workshop on Non-normal and Nonlinear Effects in Aero- and Thermoacoustics*, Munich, 18–21 June 2013.

9. Mirat C, Durox D and Schuller T. Stability analysis of a swirl spray combustor based on flame describing function. *Proc Combust Inst* 2015; 35: 3291–3298.

10. Semlitsch B, Orchini A, Dowling AP, et al. G-equation modelling of thermoacoustic oscillations of partially premixed flames. *Int J Spray Combust Dyn* 2017; 9: 260–276.

11. Bigongiari A and Heckl M. Analysis of the interaction of thermoacoustic modes with a Green's function approach. *Int J Spray Combust Dyn* 2018; 10: 326–336.

12. Crocco L. Aspects of combustion stability in liquid propellant rocket motors, part I: fundamentals. Low frequency instability with monopropellants. *J Am Rocket Soc* 1951; 21: 163–178.

13. Polifke W. Modeling and analysis of premixed flame dynamics by means of distributed time delays. *Prog Energy Combust Sci* 2020; 79: 100845.

14. Polifke W, Kopitz J and Serbanovic A. Impact of the fuel time lag distribution in elliptical premix nozzles on combustion stability. In: *The 7th AIAA/CEAS Aeroacoustics Conference and Exhibit*, Maastricht, Netherlands, 28–30 May 2001.

15. Huber A and Polifke W. Dynamics of practical premixed flames, part i: model structure and identification. *Int J Spray Combust Dyn* 2009; 1: 199–228.

16. Huber A and Polifke W. Dynamics of practical premixed flames, part ii: identification and interpretation of CFD data. *Int J Spray Combust Dyn* 2009; 1: 229–249.

17. Flohr P, Paschereit CO, van Roon B, et al. Using CFD for time-delay modeling of premix flames. In: *Proceedings of the ASME Turbo Expo 2001*, New Orleans, Louisiana, USA, 4–7 June 2001, paper no. 2001-GT-0376.

18. Flohr P, Paschereit CO and Bellucci V. Steady CFD analysis for gas turbine burner transfer functions. In: *The 41st AIAA Aerospace Sciences Meeting and Exhibit*, Reno, Nevada, USA, 6–9 January 2003, paper no. AIAA 2003-1346.

19. Schuermans B. *Modeling and control of thermoacoustic instabilities*. PhD Thesis, École Polytechnique Fédérale de Lausanne, Switzerland, 2003.

20. Schuermans B, Bellucci V, Guethe F, et al. A detailed analysis of thermoacoustic interaction mechanism in a turbulent premixed flame. In: *Proceedings of the ASME Turbo Expo*, Vienna, Austria, 14–17 June 2004, paper no. GT2004-53831.

21. Komarek T and Polifke W. Impact of swirl fluctuations on the flame response of a perfectly premixed swirl burner. *J Eng Gas Turb Power* 2010; 132: 061503.

22. Krebs W, Hoffmann S, Prade B, et al. Thermoacoustic flame response of swirl flames. In: *Volume 1: Turbo Expo 2002*, Amsterdam, The Netherlands, 3–7 June 2002, pp.333–344.

23. Gentemann A and Polifke W. Scattering and generation of acoustic energy by a premix swirl burner. In: *Proceedings of the ASME Turbo Expo 2007*, Montreal, Canada, 14–17 May 2007, pp.125–133.

24. Kaess R, Polifke W, Poinsot T, et al. CFD-based mapping of the thermo-acoustic stability of a laminar premix burner. In: *Center for Turbulence Research, Stanford University – Proceedings of the Summer Program*, 2008, pp.289–302.

25. Mensah GA, Campa G and Moeck JP. Efficient computation of thermoacoustic modes in industrial annular combustion chambers based on Bloch-wave theory. *J Eng Gas Turbines Power* 2016; 138: 081502.

26. Gopinathan SM, Iurashev D, Bigongiari A, et al. Nonlinear analytical flame models with amplitude-dependent time-lag distributions. *Int J Spray Combust Dyn* 2018; 10: 264–276.

27. Subramanian P, Blumenthal RS, Polifke W, et al. Distributed time lag response functions for the modeling of combustion dynamics. *Combust Theory Model* 2015; 19: 223–237.

28. Blumenthal RS, Subramanian P, Sujith RI, et al. Novel perspectives on the dynamics of premixed flames. *Combust Flame* 2013; 160: 1215–1224.

29. Albayrak A, Blumenthal RS, Ulhaq A, et al. An analytical model for the impulse response of laminar premixed flames to equivalence ratio perturbations. *Proc Combust Inst* 2017; 36: 3725–3732.

30. Schuller T, Durox D and Candel S. A unified model for the prediction of laminar flame transfer functions: comparisons between conical and V-flame dynamics. *Combust Flame* 2003; 134: 21–34.

31. Preetham HS and Lieuwen T. Dynamics of laminar premixed flames forced by harmonic velocity disturbances. *J Propul Power* 2008; 24: 1390–1402.

32. Steinbacher T. GFLAME. Software, Professur für Thermofluiddynamik, Technical University of Munich, 2016.

33. Karimi N, Brear MJ, Jin Seong-Ho, et al. Linear and non-linear forced response of a conical, ducted, laminar premixed flame. *Combust Flame* 2009; 156: 2201–2212.

34. Lieuwen T. Modeling premixed combustion-acoustic wave interactions: a review. *J Propul Power* 2003; 19: 765–781.

35. Mitchell IM. *A toolbox of level set methods.* Technical Report TR-2007-11, June 2007. Vancouver: University of British Columbia, Department of Computer Science.

36. Mitchell IM. The flexible, extensible and efficient toolbox of level set methods. *J Sci Comput* 2008; 35: 300–329.

Appendix 1. FTF for the generalised heat release rate law

In order to convert the approximate heat release rate law of equation (3) into the frequency-domain, we apply the Fourier transform (denoted by $\mathcal{F}$) to both sides of the equation

$$\mathcal{F}\left(\frac{Q'(t)}{\bar{Q}}\right) = \frac{1}{\tau_{\max}}\left[\underbrace{\mathcal{F}\left(n_1\int_0^{\Delta\tau}\frac{u'(t-\tau)}{\bar{u}}\mathrm{d}\tau\right)}_{Term\ 1} + \underbrace{\mathcal{F}\left(n_2\int_{\Delta\tau}^{2\Delta\tau}\frac{u'(t-\tau)}{\bar{u}}\mathrm{d}\tau\right)}_{Term\ 2} + \cdots \right.$$
$$\left. + \underbrace{\mathcal{F}\left(n_k\int_{(k-1)\Delta\tau}^{k\Delta\tau}\frac{u'(t-\tau)}{\bar{u}}\mathrm{d}\tau\right)}_{Term\ k}\right] \tag{19}$$

where t is the independent Fourier transform variable. The Fourier transform of the individual terms can be calculated analytically. For *Term 1*, we get

$$\mathcal{F}\left(n_1\int_0^{\Delta\tau}\frac{u'(t-\tau)}{\bar{u}}\mathrm{d}\tau\right) = n_1\int_0^{\Delta\tau}\frac{1}{\bar{u}}\underbrace{\mathcal{F}[u'(t-\tau)]}_{=\hat{u}(\omega)e^{i\omega\tau}}\mathrm{d}\tau = n_1\frac{\hat{u}(\omega)}{\bar{u}}\int_0^{\Delta\tau}e^{i\omega\tau}\mathrm{d}\tau \tag{20}$$

The last integral in equation (20) is straightforward to calculate

$$\int_0^{\Delta\tau}e^{i\omega\tau}\mathrm{d}\tau = \frac{1}{i\omega}\left[e^{i\omega\Delta\tau} - 1\right]_0^{\Delta\tau} = e^{i\omega\Delta\tau/2}\frac{2}{\omega}\sin\left(\frac{\omega\Delta\tau}{2}\right) \tag{21}$$

Therefore

$$\mathcal{F}\left(n_1\int_0^{\Delta\tau}\frac{u'(t-\tau)}{\bar{u}}\mathrm{d}\tau\right) = n_1\frac{\hat{u}(\omega)}{\bar{u}}e^{i\omega\Delta\tau/2}\frac{2}{\omega}\sin\left(\frac{\omega\Delta\tau}{2}\right) \tag{22}$$

In the same way, we obtain for *Term 2*

$$\mathcal{F}\left(n_2\int_{\Delta\tau}^{2\Delta\tau}\frac{u'(t-\tau)}{\bar{u}}\mathrm{d}\tau\right) = n_2\frac{\hat{u}(\omega)}{\bar{u}}e^{3i\omega\Delta\tau/2}\frac{2}{\omega}\sin\left(\frac{\omega\Delta\tau}{2}\right) \tag{23}$$

and for *Term k*

$$\mathscr{F}\left(n_k \int_{(k-1)\Delta\tau}^{k\Delta\tau} \frac{u'(t-\tau)}{\bar{u}}\mathrm{d}\tau\right) = n_k \frac{\hat{u}(\omega)}{\bar{u}} e^{(k-1/2)i\omega\Delta\tau} \frac{2}{\omega}\sin\left(\frac{\omega\Delta\tau}{2}\right) \tag{24}$$

Hence, the complete Fourier transform of equation (19) reads

$$\frac{\hat{Q}_k(\omega)}{\bar{Q}} = \left\{\frac{1}{\tau_{\max}} e^{-i\omega\frac{\Delta\tau}{2}} \frac{2}{\omega}\sin(\omega\frac{\Delta\tau}{2})[n_1 e^{i\omega\Delta\tau} + n_2 e^{2i\omega\Delta\tau} + \cdots + n_k e^{ki\omega\Delta\tau}]\right\} \frac{\hat{u}(\omega)}{\bar{u}} \tag{25}$$